

Aperture interference and the volumetric resolution of light field fluorescence microscopy

Isaac Kauvar

ikaivar@stanford.edu

Julie Chang

jchang10@stanford.edu

Gordon Wetzstein

gordonwz@stanford.edu

Department of Electrical Engineering, Stanford University, 350 Serra Mall, Stanford, CA

Abstract

Light field microscopy (LFM) is an emerging technique for volumetric fluorescence imaging, but widespread use is hampered by its poor spatial resolution. Using diffraction-based analysis we show how this degraded resolution arises because conventional LFM aims to sample four dimensions of the light field. By instead prioritizing 3D volumetric information over 4D sampling, we can optically interfere certain redundant angular samples to allow higher spatial resolution while maintaining enough angular information for depth discrimination. With this in mind, we design a number of aperture plane sampling schemes, characterize their frequency support and invertibility, and describe how their relative performance depends on the operating signal-to-noise regime. With simulations and a prototype, we demonstrate a time-sequential amplitude mask-based acquisition approach that outperforms conventional LFM in terms of both spatial resolution and axial field of view.

1. Introduction

Light field microscopy (LFM) is a technique for multiplexing volumetric information onto a two-dimensional image sensor [26]. LFM has been applied widely to fields such as neuroscience [12, 41, 40], polarization microscopy [39], and particle flow imaging [10, 15]. Although offering great promise, the current primary limitation of LFM is its poor spatial resolution relative to slower volumetric imaging techniques such as confocal and light sheet [22, 46].

In this paper, we sought to understand the fundamental sources of the poor spatial resolution of fluorescence LFM, and with that knowledge to develop approaches for improving the resolution. Although pioneering work (e.g. [28, 7]), has tried to overcome the pixel-count resolution limit of light field imaging, we build on recent related work to demonstrate how on the size scale relevant to microscopy, diffraction and noise ultimately limit performance [11, 32].

We assert that it is possible to improve upon the spa-

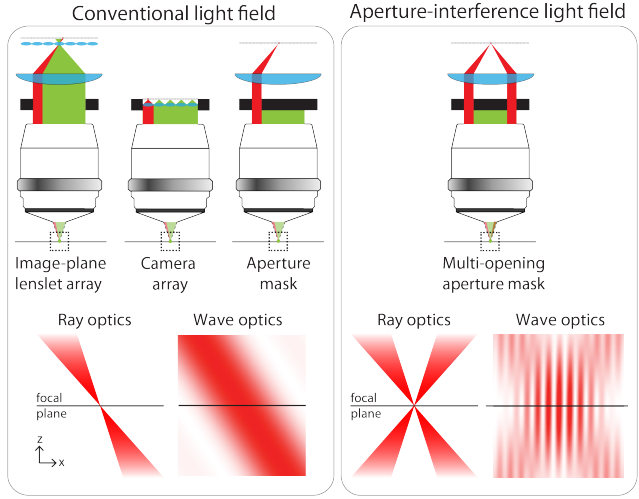


Figure 1. Aperture interference increases spatial resolution. (left) Conventional methods for recording spatio-angular samples of the light field: lenslet array, camera array, and image set captured with pinhole aperture masks [51]. Simulated wave optics pixel back-projection illustrates loss of spatial resolution not apparent with ray optics analysis. (right) Interference of light passing through multiple regions of the aperture transmits high spatial frequencies, at the cost of degraded angular information. In this paper, we will show how extraneous angular information can be traded for improved spatial resolution while maintaining axial field of view.

tial resolution of LFM due to a dimensionality gap. Conventional lenslet-based LFM is fundamentally designed to record four dimensions: two spatial dimensions, sampled by the lenslet array, and two angular dimensions, sampled by the pixel array [26]. High angular resolution is achieved by sampling from one small, compact region of the aperture at a time. For fluorescence, however, one is generally only interested in the three dimensions that parametrize the emission intensity of each specimen voxel. In particular, fluorescence emission, similar to diffuse reflection, is *incoherent* and essentially *isotropic* [35]. Incoherence implies an imaging system linear in intensity, and isotropy implies

that certain angular measurements may be redundant.

This dimensionality mismatch, or *dimensionality gap* [36, 24], suggests that there may be room to improve the spatial resolution of the LFM tomographic approach while preserving equivalent volumetric information [26]. In particular, by not limiting the sampling scheme to small, compact regions of the aperture, we conjectured that it may be possible to trade extraneous angular resolution for spatial resolution while maintaining a large axial field of view.

We thus hypothesized that by altering the spatio-angular sampling scheme, we could increase spatial resolution beyond simple pixel-count considerations. Indeed, we demonstrate that by combining angular samples in a manner that takes diffraction and interference into account while specifically targeting 3D as opposed to 4D reconstruction, one can outperform the spatial resolution achieved with the ‘conventional’ light field sampling approach that does not combine angular measurements. Our results stem from the initial observation, sketched out in Fig. 1, that in the realm of wave optics, by interfering light from across multiple regions of the aperture it is possible to record high spatial frequency information across a reasonable depth of field.

Insights In this paper, we sought to understand and improve upon the diffraction-limited resolution limits of fluorescence LFM. Our core contributions are:

- We describe the diffraction-based resolution limits of conventional LFM and analyze the resolution of alternative spatio-angular sampling strategies that incorporate aperture interference.
- We explore the impact of noise and specimen brightness on resolution performance, and compare aperture-mask based strategies with focal stack sampling.
- We propose a number of implementation designs, each with potential benefits in certain noise regimes.
- We evaluate in simulation and demonstrate with a prototype microscope the predicted enhancement of spatial resolution and axial field of view beyond LFM.

Overview of limitations So as to facilitate higher level understanding of aperture-interference and the resolution of LFM, we restricted the scope of our analysis in a few ways: we used temporal multiplexing as opposed to spatial multiplexing for recording different angular samples; to maintain analogy with fixed focal plane LFM, we limited most analysis to amplitude aperture masks; we assumed uniform one-photon illumination, and thus do not compare with coded illumination techniques such as confocal or light sheet; and we ignored scattering. In the discussion section, we describe the impact of these restrictions and how our current analysis can inform future work.

2. Related work

Light field photography Inspired by the 4D light field, a geometrical optics parametrization of the light rays emanating from a macroscopic scene [25], light field photography measures both spatial and angular information about the light entering a camera. There exist many schemes for recording a light field, also referred to as plenoptic or integral imaging, including those that use camera arrays, amplitude masks, or lenslet arrays, as schematized in Fig. 1 [52, 37, 28, 34]. The lenslet design in particular is popular because it enables single snapshot light field capture in a compact device [3, 37]. Unfortunately, with this design the choice of lenslet pitch dictates a direct tradeoff between spatial and angular resolution (and axial field of view) [37, 17]. Because of the increased flexibility for design and analysis, in this paper we use an aperture-plane amplitude mask approach for sampling the light field [28].

Light field microscopy LFM was introduced by Levoy et al. [26, 27], using a ray-optics model for reconstruction. By accurately modeling the diffractive propagation of light through a lenslet array, Broxton et al. [9] were able to increase the reconstructed resolution of lenslet based fluorescence LFM. Although pointing towards the high potential utility of LFM, the resolution was ultimately still limited and plagued by artifacts near the native focal plane. Cohen et al. [12] removed this native plane artifact by inserting a cubic phase mask in the aperture plane of the lenslet LFM, however, at the cost of decreased maximum spatial resolution. Nevertheless, the poor resolution of even state-of-the-art fluorescence LFM has become apparent in applications such as neuronal imaging [41, 46].

Super-resolution light field imaging Much previous work has focused on overcoming the pixel-count tradeoff of light field imaging [44, 47, 28, 7, 30, 34]; in the realm of microscopy, however, diffraction and not pixel-count is ultimately the limiting factor. Further, previous papers about light field resolution focused on the realm of photography and have not focused on incorporating wave-optics [37, 28, 24, 29]. Wei et al. [49] additionally explored the advantages of including aberrations, as well as irregular sampling schemes. In contrast to these works, our goal is to understand the upper bound resolution limits of LFM in the context of diffraction.

The dimensionality gap There is an initial discussion of the dimensionality gap in the paper that introduced LFM [26]. By analyzing light field sampling in the 4D frequency domain, Ng [36] proposed that the set of all full-aperture photographs, focused at any depth, lies on a specific 3D

manifold in 4D Fourier space. Dansereau et al. [13] identified this manifold as a hypercone, and showed that by digitally filtering a captured light field with a hypercone passband, one can increase the signal-to-noise ratio (SNR) of the recovered extended depth of field image.

Levin et al. [24] perform an in-depth analysis of the efficiency with which different imaging schemes sample the 3D focal manifold, including focal sweep, cubic phase mask wavefront coding, and random amplitude coded aperture. With an emphasis on recovering extended depth of field images, they show how a multi-focal ‘lattice lens’ yields reasonable resolution across a large depth of field. Although including a supplemental section devoted to derivations that incorporate wave optics, they do not incorporate these wave optics considerations into their design criteria, and conclude that if the system dimensions are large, as is generally true in photography, then a geometric model is adequate. Additionally, for the random coded aperture, they conclude that the resolution is limited by the size of each individual hole.

In contrast, we focus explicitly on application to LFM: we ask what can be gained by not aiming to separately sample light from each angle, but rather by combining multiple angular samples into each measurement. Additionally, by incorporating diffraction, we show and then leverage the non-trivial interaction, i.e. interference, between openings in a coded aperture.

Coded apertures This paper is not the first to investigate amplitude aperture coding for light field or volumetric imaging. In the graphics and computer vision communities, coded aperture photography has been applied to recording an extended depth of field image and a depth map [47, 18, 24, 54, 55, 21, 23, 20, 53], or recovering a light field [47, 34]. Sequences of images have also been used to fill in information that is missing in a single image [5, 28]. Closest to our work is programmable aperture photography, proposed by Liang et al. as a way to acquire high resolution light fields [28]. Fundamentally, this work aimed to overcome the pixel-count resolution limit by capturing a temporal sequence of images filtered by different aperture plane masks, each at the full sensor resolution. Further, to overcome the low light throughput of a single aperture pinhole, they implemented a multiplexing approach that simultaneously opened multiple pinholes. Since the target application was photography, however, unlike in this paper they ignored the resolution or depth of field consequences of different aperture designs in the context of diffraction. As diffraction is the result of a nonlinear interference effect, it cannot be modeled simply using a linear multiplexing analysis [50].

In the optics community, addressing a similar problem from a different perspective, coded aperture sequences have been used for phase space imaging of the coherence properties of a laser beam, or for localizing sparse point emitters in

3D in scattering media [48, 31, 32]. Although briefly hinting at the resolution improvements attainable with a multiplexing approach, Liu et al. [32] focus on the potential light throughput and compressive sensing advantages of such an approach. In related work, Chang et al. [11] use apertures of multiple sizes to increase the resolution of a macroscopic reconstructed 4D Wigner distribution, but do not investigate how such an approach can benefit volumetric microscopy. Annular pupil coding microscopy has been discussed in the context of increasing planar resolution or depth of field [43, 42]. Wavefront coded angular tomographic sampling has been used to reconstruct macroscopic 3D volumes [33]. We extend these works by using the coded aperture framework to understand the diffraction-induced limits specifically of 3D volumetric fluorescence LFM.

Incoherent volumetric imaging Before delving into an analysis of LFM, it is worth highlighting that LFM is just one of many possible solutions to the general problem of incoherent volumetric imaging, also known as focal tomography. Focal stack deconvolution is the most obvious method, in which a temporally or spatially multiplexed sequence of images focused at different planes in the sample are captured and then jointly deconvolved [4, 1, 2]. However, focal stack techniques run into trouble when imaging large axial fields of view with a limited image budget [8]. Image space coding techniques have been proposed as an alternative, but have not yet been widely transferred to the microscopy realm [8]. In contrast to these techniques that use phase coding to adjust or extend focus, and in seeking an understanding of the limits of specifically LFM, we investigate the diffraction-imposed limits of spatio-angular sampling based microscopy that maintains a single primary plane of focus; we do, however, also make a comparison with focal stack and demonstrate when our approach may be advantageous.

3. Analysis

Aperture interference We consider both lateral and axial resolution in the 3D spatial frequency domain, (k_x, k_y, k_z) . To measure imaging performance we use the incoherent *defocus optical transfer function (OTF)*, defined as the 3D Fourier transform of the incoherent point spread function (PSF) [43, 6]. By describing axial resolution in addition to the commonly analyzed lateral resolution, the 3D OTF can serve as a basis for comparing aperture mask designs for volumetric imaging applications.

A useful feature of the defocus OTF is that it can be computed or visualized directly from a given aperture mask, without even computing the associated PSF. The defocus OTF is the 3D autocorrelation of the *generalized* aperture [35]. The generalized aperture extends the 2D coherent am-

plitude transfer function, $ATF(k_x, k_y)$, to 3D by incorporating the phase associated with the propagation of light as it defocuses. In our case, $ATF(k_x, k_y)$ is just the aperture mask function. The generalized aperture, $ATF(k_x, k_y, k_z)$ is then the projection of the 2D aperture mask onto the surface of a spherical shell in (k_x, k_y, k_z) space, also known as the Ewald sphere, as shown in the top of Fig. 2.

$$ATF(\mathbf{k}) = ATF(k_x, k_y) \delta(k_z - \sqrt{k^2 - k_x^2 - k_y^2}) \quad (1)$$

$$OTF(\mathbf{k}) = ATF(\mathbf{k}) \star_3 ATF(\mathbf{k}) \quad (2)$$

where $\mathbf{k} = (k_x, k_y, k_z)$, $k = n2\pi/\lambda$ is calculated from the wavelength λ in refractive index n , and \star_3 is 3D autocorrelation. See Supplement for more detail.

The defocus OTF enables fast assessment of the merits of various aperture mask schemes. This is most easily illustrated with the toy model in Fig. 2 of a 1D aperture and a specimen spanning just one lateral and one axial dimension. As a first analysis, we tested our hypothesis that the *interference* from an aperture with two pinholes would transmit more information than the low pass filter of a single pinhole.

In Fig. 2 we compare four 1D aperture mask configurations: 1) a single pinhole, or the *LF-pinhole* sweep, which emulates conventional LFM; 2) two pinholes moved symmetrically about the optical axis, or the *symmetric* sweep; 3) two pinholes with the first pinhole fixed at the aperture edge, and the second pinhole scanned across the aperture, or the *anchored* sweep; and 4) two pinholes scanned through all combinations of aperture locations, or the *complete* sweep. In Fig. 2 we plot for each configuration the defocus OTF support of one aperture mask in the sequence, the union of the defocus OTF of all aperture masks in the sequence, and an example PSF. A few conclusions emerge:

1) The interference of light passing through two pinholes enables detection of lateral and axial spatial frequencies wholly inaccessible with LF-pinhole, suggesting the potential of higher resolution than is possible with standard LFM. However, as is the case with all single objective, widefield illumination techniques, we observe that LFM and all aperture mask techniques are subject to the missing cone problem and an inability to perform true optical sectioning [35].

2) Scanning all possible configurations of two pinholes, in the complete sweep, samples all possible spatial frequencies that are transmitted through a fully open aperture. However, the number of images required to capture this sweep is large compared to the other methods, and is potentially inefficient for capturing volumetric information.

3) The anchored and symmetric sweeps each sample a subset of the possible frequencies, but do so differently: the anchored sweep samples all k_z values at least once, whereas the symmetric sweep samples only small k_z values, and thus does not provide axial resolution. Asymmetry about the optical axis is thus important for achieving axial resolution.

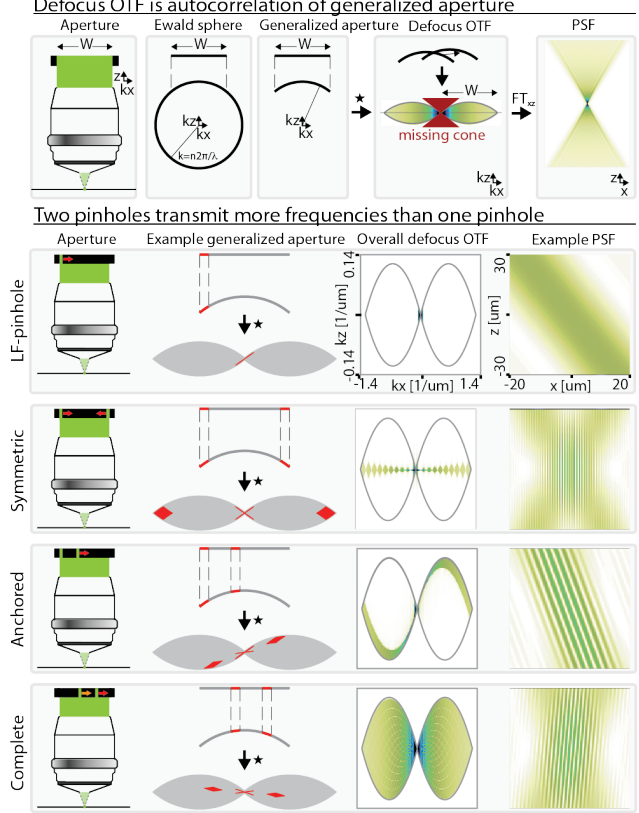


Figure 2. Defocus OTF as an analysis tool. Here we show the 2D x-z planar case. (top) The defocus OTF can be derived directly from an aperture mask, as the autocorrelation of the generalized aperture. The 3D PSF is the 3D Fourier transform of the 3D defocus OTF. (bottom) Increased spatial frequency content is accessible with a two-pinhole aperture mask. First column schematizes each aperture sequence; second column demonstrates for an example mask the OTF coverage (in red) superimposed on the OTF of a fully open aperture (in gray); third column plots the overall defocus OTF coverage of the mask sequence; and fourth column shows the PSF corresponding to the example mask.

Scanned aperture mask design principles In the previous section, we observed promising hints that the two-pinhole aperture could yield improvements over LF-pinhole capture. To better define the advantages and disadvantages of each mask sequence, however, we need to better describe the desired characteristics of a sequence of defocus OTFs corresponding to a sequence of aperture masks. Three primary properties stand out:

1) Frequency space coverage The aperture mask sequence should transmit as many lateral and axial spatial frequencies as possible.

2) Frequency space invertibility The samples must have diversity to enable separation of different frequency components, particularly in the axial direction. As an example, one

image from a fully open aperture focused at a single plane *does* sample all spatial frequencies, but does not contain 3D information (see Supplement for further discussion).

Invertibility is also related to the SNR of each frequency. As we will explore, SNR can be distributed unevenly: certain aperture mask sequences may provide better SNR at higher spatial frequencies, but worse performance at lower frequencies. The choice of aperture sequence may thus depend on properties of the specimen to be imaged.

We can quantify this design principle using the singular values of the frequency domain measurement matrix. Let $M \in \mathbb{C}^{n_{k_x} n_{k_y} N \times n_{k_x} n_{k_y} n_{k_z}}$ be the measurement matrix, where N is the number of aperture masks in a sequence. We normalize M appropriately to account for the fact that some aperture masks transmit less light than others. See Supplement for a more detailed derivation.

If $N = n_{k_z}$, then M is a square matrix and potentially invertible. We can use the singular value decomposition (SVD) to estimate the invertibility of M , or more specifically, to estimate how many separable components M is capable of encoding. The singular values represent the gain with which inputs to a matrix are filtered. In particular, one can estimate the ‘rank’ of a matrix, or the number of linearly independent columns, by counting the number of singular values above a threshold:

$$R = \sum_i \mathbf{1}[|\sigma_i(M)| > T] \quad (3)$$

where R is our measure of invertibility, $\mathbf{1}$ is the indicator function which takes the value 0 if the argument is false and 1 if it is true, $\sigma_i(M)$ is the i th singular value of M , and T is the appropriate threshold. In our case, that threshold is determined by the noise characteristics of the system, which we will describe more in following sections. In this context, the rank of the frequency domain measurement matrix M conveys information about the spatial resolution and depth of field of the reconstruction. See Supplementary Fig. S2 for further discussion.

3) Minimal number of images. While the complete sweep approach of Fig. 2 satisfies the first two criteria, it requires an unwieldy number of images - approaching $N^2!$ images for a 2D aperture, whereas LF-pinhole requires only N^2 . Our goal is thus to improve upon the complete sweep by finding aperture mask sequences that match its frequency coverage and invertibility while minimizing the number of images required for volumetric reconstruction.

4. Aperture mask design

Efficient aperture-interference codes We define an Aperture-interference Light Field (ALF) microscope as one that harnesses spatio-angular sampling for volumetric imaging, like conventional LFM, but that also utilizes interference from multiple points across the aperture to increase

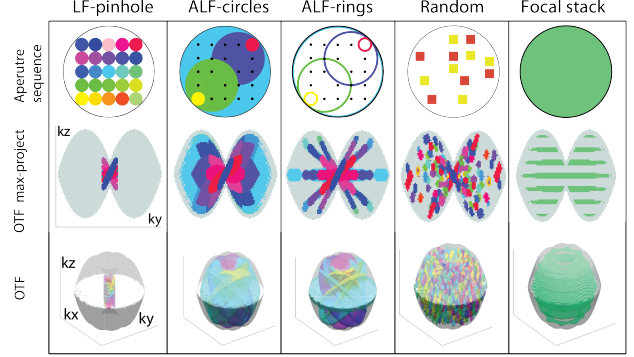


Figure 3. Scanned aperture mask design comparison. (top row) Schematic showing a subset of the aperture mask patterns for each indicated sequence. Each color represents a different mask. (middle row) Max-projection across k_x of 3D OTF support for each sequence. (bottom row) Rendering of 3D OTF support. Colors correspond with those in top row. Each sequence consists of 25 masks. Focal stack OTF is the real component of the OTF for a single image (the absolute value, however, solidly fills in the entire gray region). For the other four designs, each color indicates the support corresponding to a single mask in the capture sequence. These mask sequences are used for the next two figures as well.

spatial resolution while preferably maintaining angular resolution. The complete sweep of Fig. 2 is an extreme example of ALF. It essentially measures one (k_x, k_y, k_z) sample of the defocus OTF at a time, plus a DC term. One can improve upon it by determining which measurements can be taken simultaneously without substantially degrading the performance of the volume recovery. We hypothesize this increased efficiency to be possible because of the dimensionality gap from a 4D light field to a 3D volume. We discuss three specific approaches below. For comparison, we refer to the scanned aperture analog of conventional LFM as LF-pinhole, which uses same-size non-overlapping circular apertures spaced on a rectilinear grid. For a reader familiar with light field photography, LF-pinhole directly captures 2D planes at fixed u and v of the 4D light field of (x, y, u, v) , where u and v are discretized based on the pinhole sampling grid. With ALF, we sample more complicated manifolds of the 4D space, since we are ultimately trying to find $f(x, y, z)$, not $f(x, y, u, v)$.

ALF-circles: The first approach extends the tomographic sampling of LF-pinhole, but combines short depth of field, high lateral resolution images with large depth of field, high axial resolution images [11]. In particular, ALF-circles follows this recipe: for each of the same grid locations as the centers of LF-pinhole openings, the aperture mask is an open circle centered on that grid location but with a diameter large enough to touch the border of the full aperture. Hence the central grid position uses the full aperture while off-axis grid positions use smaller aperture openings. As

shown in Fig. 3, by visual inspection, this sequence provides high coverage and reasonable invertibility.

ALF-rings: The second design takes advantage of the isotropic quality of fluorescent emission to yield a more efficient 2D version of the complete sweep. This is similar to ALF-circles, except that centered on each grid location we use a thin ring instead of an open circle. This records large depth of field, angled Bessel beam projections through the sample (whereas LF-pinhole produces Gaussian beam projections) [38, 16]. The ring width trades off depth of field for light throughput. As evident in Fig. 3, in contrast to ALF-circles, each ALF-rings aperture samples a thin k_z extent for each k_x value, providing reasonable coverage and invertibility. The sampling is similar to that of the complete sweep, but multiple k_x values are measured simultaneously, and thus fewer overall images are required. Future designs would likely benefit from dithering the center positions so that they do not lie on a perfect grid. In the Supplement, we also discuss simplified variants of this scheme.

Random masks: For comparison, we include the random mask design of [32], which consists of a sequence of non-overlapping random masks, such that every point in the aperture is sampled once throughout the sequence. As seen in Fig. 3, this offers a speckled sampling of the OTF. The irregular sampling of this approach potentially has benefits for minimizing aliasing [9, 49], although with pupil plane sampling aliasing likely plays a less noticeable role. For later simulations, we also analyze a random mask sequence where for each mask, 50% of the aperture is open, which has overlap between masks but transmits more light.

Noise In Fig. 3, we visually examine the high signal (essentially noise-free) frequency support of the above three mask designs, compared against LF-pinhole and focal stack. We observe that ALF-pinhole, ALF-rings, and random mask offer significantly more coverage than LF-pinholes, as well as a degree of invertibility.

In the low-light realm of fluorescence microscopy, however, Poisson noise is important in determining what frequencies are actually recoverable. For scientific cameras, read noise is generally negligible. Because Poisson noise at each pixel is independent of the noise at neighboring pixels, the noise power spectrum is flat across spatial frequencies with a mean-square magnitude equal to the mean sensor pixel value. In the Supplement, we validate this with a Monte Carlo simulation.

We can explicitly compute the mean-square SNR at each spatial frequency as a function of specimen brightness for each mask, using the information theory definition [45]:

$$SNR(\mathbf{k}) = \frac{P_{signal}}{P_{noise}} = \frac{|A \cdot N \cdot OTF(\mathbf{k})/OTF(\mathbf{0})|^2}{A \cdot N} \quad (4)$$

where P_{signal} is the mean-square signal intensity per frequency, P_{noise} is the mean-square noise intensity per frequency, A is the fraction of the full aperture that is open for a given aperture mask, and N is the mean number of photons per sensor pixel with the aperture fully open (which quantifies specimen brightness consistently across masks).

To analyze the impact of SNR, we selected a reasonable though arbitrary threshold of $SNR(\mathbf{k}) \leq 1$ as the value at which signal is difficult to recover. This occurs when $|A \cdot N \cdot OTF(\mathbf{k})/OTF(\mathbf{0})| \leq \sqrt{A \cdot N}$. Thus, for a given aperture, $\sqrt{A \cdot N}$ can be seen as a noise floor to compare against the signal at each frequency. This is not a hard boundary, and key observations are insensitive to the exact value.

We can also use this concept of the Poisson noise floor to establish the threshold T for computing the invertibility R of an aperture mask sequence, as defined in Eq. 3. In particular, if N is the mean number of photons arriving at a sensor pixel during one exposure for a fully open aperture, then \sqrt{N} is the noise threshold in the frequency domain. Let A_q be the fraction of the full aperture that is open for a given aperture mask q . As described in the frequency space invertibility section, we incorporate A_q directly into computation of the singular values, and thus the signal associated with a singular value s_i , which is computed jointly across all masks, is $N \cdot s_i$. Across all of the measurements in a sequence of Q images, the average noise floor for the images in the mask sequence is $\sum_q \sqrt{A_q \cdot N}/Q$. Thus, if we set the signal from a singular value to equal the average noise floor, $N \cdot s_i = \sqrt{N} \cdot \sum_q \sqrt{A_q}/Q$, then, solving for s_i :

$$T = (\sum_q \sqrt{A_q})/(Q\sqrt{N}) \quad (5)$$

is interpreted as the noise threshold for singular values.

In the top of Fig. 4, we plot invertibility R as a function of specimen brightness, according to Eqs. 3 and 5, and assuming equal exposures per mask. What becomes clear is that different masks perform best in different brightness regimes. Whereas for low photon (high relative noise) regimes the masks with larger openings perform better, for larger photon counts, it is worth masking some of the aperture to gain invertibility. For reference, imaging a dim specimen susceptible to photobleaching at tens of Hz generally yields photon counts below 10^3 photons, whereas brighter, more robust specimens can fill the $10^4 - 10^5$ photon dynamic range of the camera. Interestingly, random masks with 50% open aperture perform quite well, particularly for higher photon counts. Here, though, we find that focal stack offers the most information across nearly all reasonable signal regimes.

In the bottom of Fig. 4, we plot the results with a slightly different normalization of the OTFs, as a proxy for a single-snapshot implementation – the ultimate goal. Here, instead of assuming that each mask in the sequence is presented for the same exposure, we assume that we have an ideal beam-

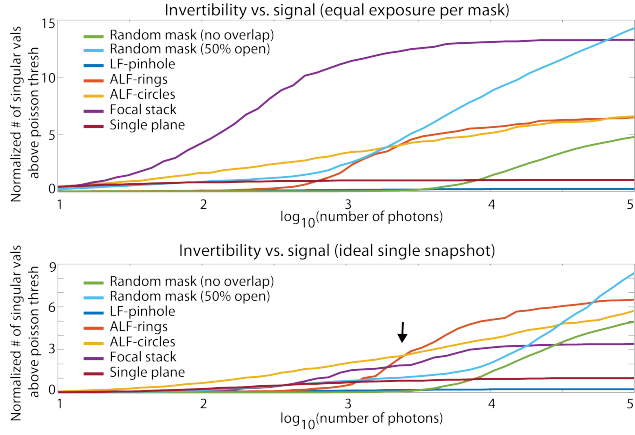


Figure 4. Frequency space invertibility depends on the signal-to-noise regime. (top) Assumes equal exposure time for each mask in the sequence. (bottom) Assumes ideal optical device exists to split light for a single snapshot capture, and thus accounts for overlap between masks in a sequence. Invertibility is plotted as a function of average number of photons per pixel (with the aperture fully open), assuming Poisson noise. Values were normalized to the maximum achievable with ‘single plane’, which corresponds to 25 images with an open aperture, all focused on the same plane.

splitter which simultaneously redirects light from a single exposure according to each of the aperture masks. As an example, if one part of the aperture is covered by five aperture masks, only 1/5 of the photons through that region are assigned to each corresponding image. To simulate this, we additionally normalize each OTF based on the amount of overlap that the corresponding aperture mask has with all other masks in the sequence. Further, we modify Eq. 5 so that A_q incorporates the degree of overlap for each mask. Because focal stack, 50% overlap random masks, and ALF-circles have a large amount of overlap, whereas ALF-rings does not, we observe a change in relative performance. In particular, for low-photon counts, ALF-circles performs best. For larger photon counts ALF-rings performs best (see black arrow). Based on these results and their implications for future snapshot implementations, we focused our subsequent investigation on focal stack, ALF-rings, and ALF-circles.

In the top of Fig. 5, again exploring the non-single snapshot case, we explicitly plot the SNR (Eq. 4) along the k_x axis, max-projected across k_z and across all masks in each sequence. The conclusion here is that for high signal, and thus low relative Poisson noise, ALF-rings provides higher SNR at the highest frequencies (see red arrow). For lower signal, as the information at these high frequencies becomes washed out by the noise, the mid-frequency strength of sequences with larger aperture openings offer more of an advantage. Finally, ALF-circles always performs better than LF-pinholes. Thus, depending on sample brightness and the

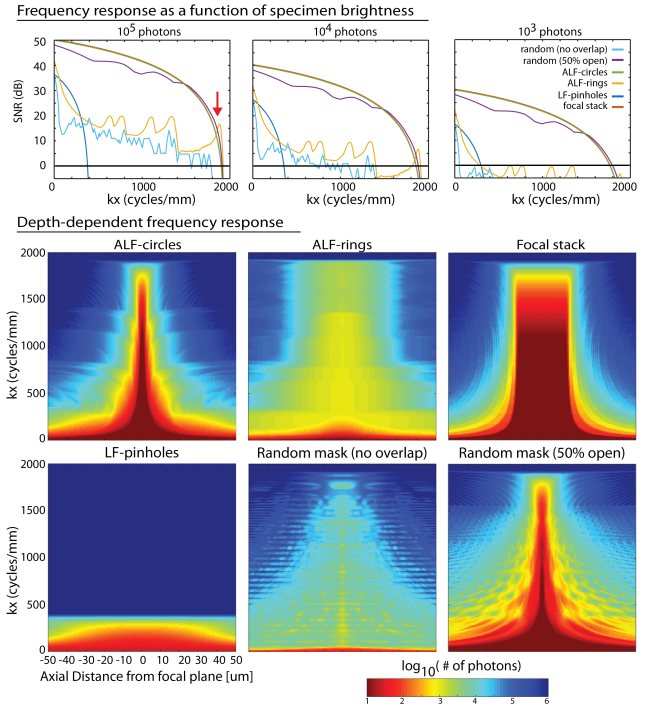


Figure 5. Frequency response as a function of noise and depth. For the same aperture mask sequences as in Fig. 4, with equal exposure per mask. (top) Signal-to-noise ratio at different specimen brightness values, along the k_x axis of the OTF, max-projected across images in each sequence. Photon count is the average number of photons per pixel with the aperture fully open. Red arrow indicates where ALF-rings outperforms all other masks at the highest spatial frequencies. (bottom) Depth-dependent OTF as a function of specimen brightness, max-projected across k_y and all images in each sequence. Color indicates specimen brightness at which the signal power is above Poisson noise power.

relative importance of different frequency bands, the performance of different aperture mask sequences varies.

Depth-dependent OTF Intuition derived from using the defocus OTF (Eq. 2) can be augmented by also plotting the depth dependent OTF, or simply the Fourier transform of $OTF(k_x, k_y, k_z)$ along the k_z direction. This provides the lateral resolution as a function of depth from the focal plane, as shown in Fig. 5 (here assuming equal exposure time per mask). We take noise into account according to Eq. 4 by computing $H = |\sqrt{A} \cdot OTF_z(k_x, k_y)/OTF_z(\mathbf{0})|^2$, setting $SNR = 1$, and thus plotting $\log_{10}(1/H)$, max-projected across all masks in a sequence. The color then represents the number of photons per pixel (with a fully open aperture) necessary for $SNR(k_x, k_z) \geq 1$. We find that for a limited number of images, focal stack offers the strongest performance within a small axial range, whereas for bright enough specimens, other approaches such as ALF-rings and

random mask can offer good performance across a larger axial range.

In the next sections, we test the performance of these aperture mask designs for reconstructing volumes in simulation and with a hardware prototype and explore the consequences of different specimen brightness levels.

5. Results

5.1. Simulation

Forward model and reconstruction Incoherent fluorescent image formation can be described by filtering in the pupil plane with the 2D depth-dependent $OTF_z(k_x, k_y)$ for each depth z , followed by axial projection onto the camera sensor to sum contributions from each depth. We discretize the sample volume into n_v voxels and the camera sensor into n_p pixels. For a sequence of Q images, we apply the forward model $\mathbf{I} \sim \text{Pois}(A\mathbf{x} + \mathbf{b})$, where $\mathbf{I} \in \mathbb{R}^{n_p Q}$ is the vectorized stack of sensor images, $\mathbf{x} \in \mathbb{R}^{n_v}$ is the vectorized discrete sample volume, $\mathbf{b} \in \mathbb{R}^{n_p Q}$ is the vectorized background signal, and $A \in \mathbb{R}^{n_v \times n_p Q}$ is the measurement matrix composed by

$$A = P_z F_b^{-1} K F_x, \quad (6)$$

where $F_x \in \mathbb{C}^{n_v \times n_v}$ takes the 2D discrete Fourier transform (DFT) of each z-slice of the volume, $K \in \mathbb{C}^{n_v Q \times n_v}$ is a stack of diagonal matrices that perform element-wise multiplication with $OTF_z^{(q)}$ for each depth z and each aperture mask q , $F_b^{-1} \in \mathbb{C}^{n_v Q \times n_v Q}$ is a block diagonal DFT matrix that takes the inverse 2D DFT along k_x and k_y , and $P_z \in \mathbb{R}^{n_p Q \times n_v Q}$ applies a projection along z .

We solve for the most likely \mathbf{x} given \mathbf{I} and estimated \mathbf{b} with the common Richardson-Lucy iterative updates:

$$\mathbf{x}^{(j+1)} = \text{diag}(A^H \mathbf{1})^{-1} \text{diag}[A^H \text{diag}(A\mathbf{x}^{(j)} + \mathbf{b})^{-1} \mathbf{I}] \mathbf{x}^{(j)} \quad (7)$$

where A^H is the adjoint of A . See Supplement for details.

Simulation results We began by testing our aperture sequence designs in simulation. We compared three cases, each with 25 aperture masks centered on the corresponding 25 locations of a 5×5 square grid: (1) LF-pinholes, (2) ALF-circles, and (3) ALF-rings. Further, since random aperture masks have been used in similar work [28, 24, 32], we additionally compared the performance of 25 random binary aperture masks. Here, because Fig. 4 implied that non-overlapping random masks only work for very bright signal levels, we used random masks that each had 50 percent light transmission. Our hypothesis from previous analyses was that LF-pinholes would have the worst resolution, and that for bright samples ALF-rings would offer the highest resolution across the largest axial field of view.

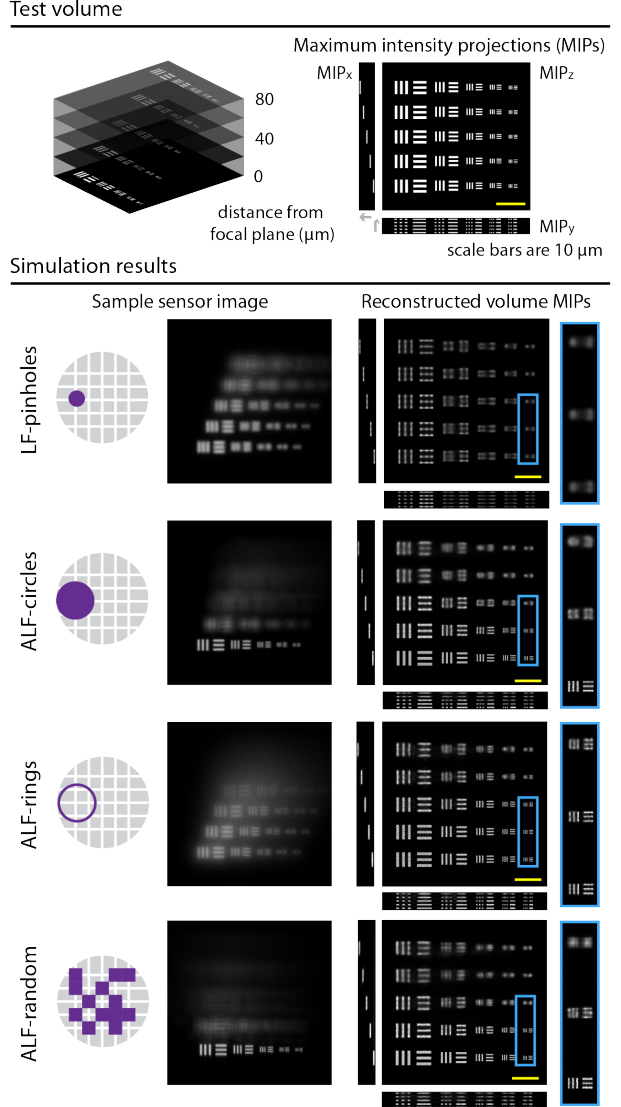


Figure 6. Simulation results showing the test volume, sample sensor images with Poisson noise for each of the aperture mask schemes, and maximum intensity projections (MIPs) of the reconstructed volumes. The volume ($1024 \times 1024 \times 15$) consisted of non-overlapping test resolution bars every third slice, with $6.67 \mu\text{m}$ between each slice. All scale bars measure $10 \mu\text{m}$.

As shown in Fig. 6, we simulated sensor images and reconstructions for a test resolution chart volume. All sensor images had equal bright (10^6 photons) total intensities with Poisson noise applied. The reconstructions were run for 2000 iterations, throughout which the mean-square-error to the test volume monotonically decreased. While the individual ALF-ring sensor images possessed more background blur, they also contained high frequency information not present in the pinhole images. We observe that ALF-rings obtains the best results of the four cases, as it resolves the

smallest 0.5 μm wide bars even at 40 μm from the focal plane and the next-smallest 0.8 μm wide bars to at least 80 μm from the focal plane. ALF-circles outperformed LF-pinholes near the focal plane while matching LF-pinholes farther from the focal plane. These results supported our intuition and hypothesis, and we were thus encouraged to implement a prototype.

5.2. Experimental prototype

Optical setup We used a commercial top-illuminated epifluorescence microscope with a 20x 0.5 NA objective (Olympus) and a 4f system extension, as shown in the top of Fig. 7. Aperture masks printed on transparencies (Fine-line printing) were mounted on a motorized rotation mount (Thorlabs) placed at the conjugate pupil plane. Although one could use a spatial light modulator instead of physical masks, we decided against it at this stage due to the potential light loss and diffraction effects. A drawback of our implementation is that while convenient for mask designs with symmetry, that could easily be calibrated, it was not as straightforward for us to test random mask designs. We leave empirical testing of those designs for future work. Images were taken with the Hamamatsu ORCA-Flash4.0 V2 digital sCMOS camera. Exposure times were set to nearly saturate the sensor for each mask (over 10^4 photons). For more details see Supplement.

USAF resolution target results We captured aperture-mask sequences (13 masks per scheme) of a USAF 1951 resolution target (Edmund Optics) placed on top of a fluorescent slide at a series of defocus distances from objective's focal plane. We reconstructed the target individually at each defocus position, as seen in Fig. 7. Results from both ALF configurations surpass those of LF-pinholes near the focal plane. Up to at least 100 μm from the focal plane, ALF-rings continues to outperform the other aperture mask schemes, due to the larger depth of field Bessel PSFs [16].

Notably, ALF-rings also outperforms state-of-the-art lenslet-based LFM results (see Fig. 5 in [9]), which uses the same 20x/0.5NA objective and resolution chart, but achieves resolution in group 9 only out to 15 μm from the focal plane, as opposed to 30 μm for ALF, and resolution in group 8 only out to 50 μm , as opposed to 100 μm for ALF.

Fluorescent pollen grain results Our next specimen was a slide of autofluorescent pollen grains (Celestron). The volume reconstructions are shown in Fig. 8 and Fig. S6. In this case, results with ALF-circles surpass those with ALF-rings. The pollen grain was a dim sample compared to the resolution chart, corresponding to around 10^3 photons per pixel in Fig. 4. While with ALF-rings only pockets of high frequencies were above the noise threshold, ALF-

circles maintained $SNR \geq 1$ for a continuous range of middle frequencies. In addition, the specimen was only around 40 μm thick in total, so the disparity at farther distances from the focal plane was not relevant. Further, as expected at this specimen brightness, focal stack with deconvolution outperformed all amplitude mask based methods.

6. Discussion

We began this paper by investigating the diffraction-imposed limits on the axial and lateral resolution of LFM, in search of scanned aperture angular sampling schemes that could yield improved spatial resolution with an equivalent axial field-of-view. Using the 3D OTF, we discovered that very little of the total information transmitted through the microscope objective is recovered with existing light field techniques, particularly those that sub-aperture sample. Based on this analysis, we developed design principles for utilizing more of the information transmitted through the objective. From these principles, we designed the Aperture-interference Light Field (ALF) schemes and showed that they provide higher resolution volumetric images than previous LFM designs [9, 30], both in simulation and experimentally. We also demonstrate how various assumptions and parameters yield changes in relative performance between focal stack and amplitude aperture mask schemes.

Whereas conventional LFM records fixed width Gaussian beam projections at different angles through a specimen, ALF-circles and ALF-rings record projections with varying beam-waists. This decouples some of the trade-off between depth of field and spatial resolution of standard LFM, enabling recovery of more spatial frequency content. Intriguingly, when considering the tradeoffs of a potential single-snapshot design, both ALF-rings and ALF-circles offer advantages compared even to focal stack (see bottom of Fig. 4).

As alluded to earlier, we limited the scope of our analysis in a number of ways that deserve further discussion. First, we rely on a sequential acquisition strategy, because it is more intuitive to analyze and easier to implement with a proof-of-concept prototype. Although for bright specimens sequential ALF may fill a niche between high-resolution but slow methods such as confocal, and low-resolution but fast methods such as LFM, there are a number of paths to achieving a single-snapshot ALF-inspired configuration (in line with the bottom of Fig. 4), including: 1) a specially designed pupil plane phase mask, fabricated as in [1] or SLM-generated as in [48], that can simultaneously implement multiple overlapping lenses and gratings to spatially multiplex images corresponding to different aperture masks; 2) a mirror or beamsplitter based implementation similar to [18]; 3) a beamsplitter approach that enables the simultaneous application of different masks to copies of the image; 4) a lenslet array using lenslets with curved focal

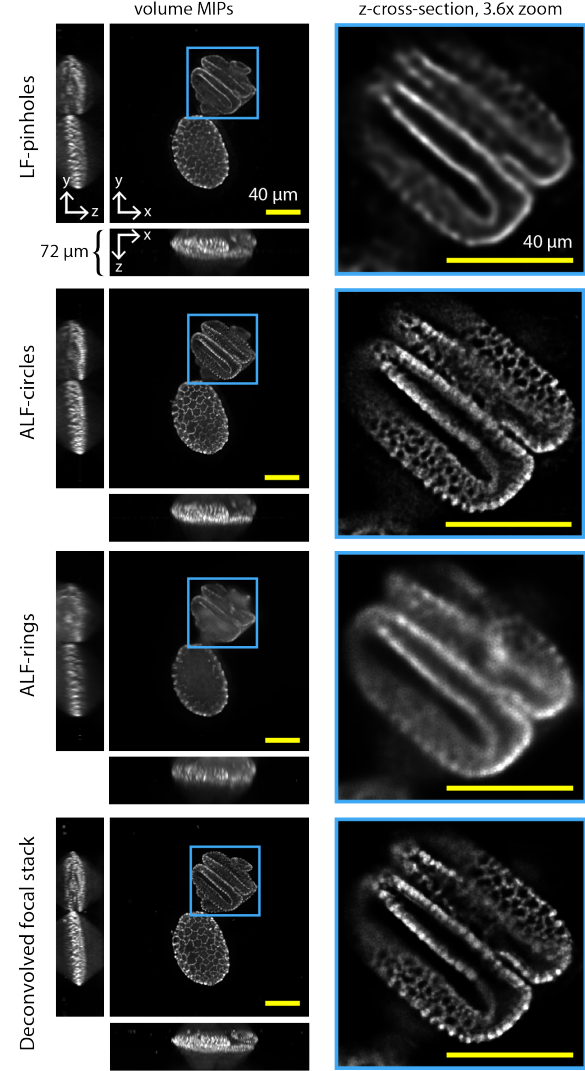
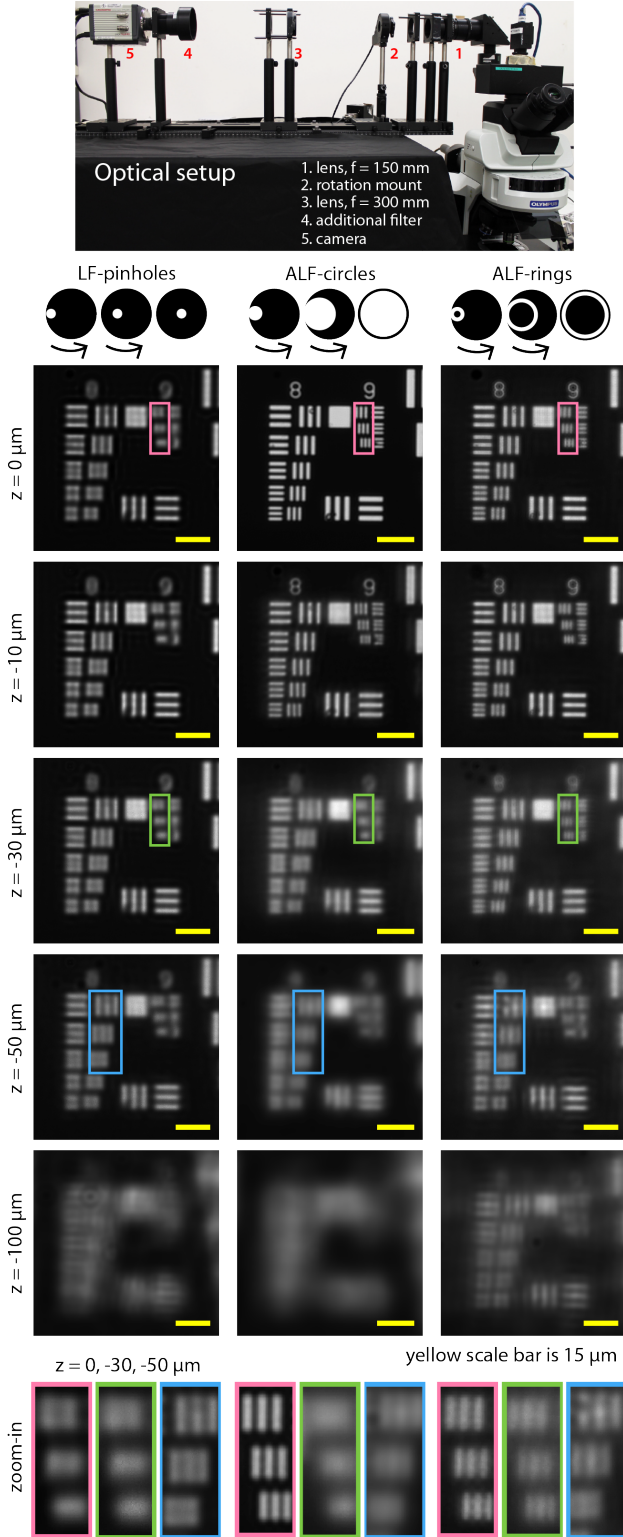


Figure 8. Deconvolved volumes of experimentally captured pollen grain data with LF-pinholes, ALF-circles, ALF-rings, and focal stack showing (left) Maximum intensity projections (MIPs) of the reconstructed volume and (right) zoomed-in z -cross-sections (at focal plane) of reconstructed pollen grains. For pollen grain MIPs, the aspect ratio $x:y:z$ is 1:1:3.2. Yellow scale bars measure 40 μm .

planes such that pixels behind a single lenslet sample light through possibly non-disjoint subsets of the aperture plane.

To understand the fundamental resolution limits of LFM, we excluded scattering from our analysis. For many specimens, including larval zebrafish and cell cultures, this is a reasonable assumption [12]. It is of interest for future work to consider the extent to which scattering affects the dimensionality gap and the assumption of angular redundancy, especially in the context of recent associated work [31].

Finally, we note that in order to maintain a direct analogy with existing light field systems, our analysis was limited

to binary amplitude-only aperture masks and uniform epi-illumination. Future work should investigate variable phase and amplitude aperture profiles, including exploring other techniques for recording high depth of field projections beyond a Bessel beam, such as a cubic phase mask [14, 33]. Further, the OTF analysis presented here lends itself toward investigating how active illumination such as structured illumination can help expand the spatial frequency support of pupil coded light field techniques [19]. In particular, by surpassing the small-aperture induced resolution bottleneck of the LFM approach, we shed light on how other aspects of LFM become the primary limiting factors, providing targets of future work: that LFM relies on uniform widefield illumination, and that it concentrates its collection of information from around a single focal plane.

7. Conclusion

Light field fluorescence microscopy (LFM) accomplishes volumetric imaging across a large axial field of view by recording many angular perspectives of a specimen. Each perspective contains high angular resolution and a large depth of field because it effectively only samples from a small region of the aperture; for the exact same reason, however, each perspective suffers from poor diffraction-limited spatial resolution. We find that this ultimately lies at the heart of why LFM has poor optical resolution. By noting that LFM was fundamentally designed to sample four spatio-angular dimensions, but fluorescence microscopy only seeks recovery of three spatial dimensions, we set out to determine whether by merging redundant angular samples it would be possible to improve the diffraction-limited resolution of LFM. Using the 3D OTF and amplitude aperture masks, we show that by considering the interference of light that passes through different parts of the aperture, it is indeed possible to develop sampling schemes that achieve higher spatial resolution across an equivalent axial field of view as compared with both conventional LFM and existing amplitude aperture codes. In concert, our findings provide a crucial step towards high resolution, snapshot volumetric microscopy.

8. Acknowledgements

The authors thank Marc Levoy, Michael Broxton, Donald Dansereau, Samuel Yang, Matthew Arnison, Ren Ng, John Pauly, and Anat Levin for insightful discussions, Olympus Corporation for access to the microscope, and the reviewers for their comments. IK and JC were each supported by an NSF GRFP.

References

- [1] S. Abrahamsson, J. Chen, B. Hajj, S. Stallinga, A. Y. Katsov, J. Wisniewski, G. Mizuguchi, P. Soule, F. Mueller, et al. Fast multicolor 3d imaging using aberration-corrected multifocus microscopy. *Nature methods*, 10(1):60–63, 2013.
- [2] S. Abrahamsson, R. Ilic, J. Wisniewski, B. Mehl, L. Yu, L. Chen, M. Davanco, L. Oudjedi, J.-B. Fiche, B. Hajj, et al. Multifocus microscopy with precise color multi-phase diffractive optics applied in functional neuronal imaging. *Biomedical optics express*, 7(3):855–869, 2016.
- [3] E. H. Adelson and J. Y. A. Wang. Single lens stereo with a plenoptic camera. *PAMI*, (2):99–106, 1992.
- [4] D. A. Agard. Optical sectioning microscopy: cellular architecture in three dimensions. *Annual review of biophysics and bioengineering*, 13(1):191–219, 1984.
- [5] A. Agrawal, Y. Xu, and R. Raskar. Invertible motion blur in video. volume 28, page 95. ACM, 2009.
- [6] M. R. Arnison and C. J. Sheppard. A 3d vectorial optical transfer function suitable for arbitrary pupil functions. *Optics communications*, 211(1):53–63, 2002.
- [7] T. E. Bishop, S. Zanetti, and P. Favaro. Light field superresolution. In *ICCP*, pages 1–9. IEEE, 2009.
- [8] D. J. Brady and D. L. Marks. Coding for compressive focal tomography. *Applied optics*, 50(22):4436–4449, 2011.
- [9] M. Broxton, L. Grosenick, S. Yang, N. Cohen, A. Andelman, K. Deisseroth, and M. Levoy. Wave optics theory and 3-d deconvolution for the light field microscope. *Optics express*, 21(21):25418–25439, 2013.
- [10] M. F. Carlsohn, A. Kemmling, A. Petersen, and L. Wietzke. 3d real-time visualization of blood flow in cerebral aneurysms by light field particle image velocimetry. In *SPIE Photonics Europe*, pages 989703–989703. SPIE, 2016.
- [11] J. Chang, I. Kauvar, X. Hu, and G. Wetzstein. Variable aperture light field photography: overcoming the diffraction-limited spatio-angular resolution tradeoff. In *CVPR*. IEEE, 2016.
- [12] N. Cohen, S. Yang, A. Andelman, M. Broxton, L. Grosenick, K. Deisseroth, M. Horowitz, and M. Levoy. Enhancing the performance of the light field microscope using wavefront coding. *Optics express*, 22(20):24817–24839, 2014.
- [13] D. G. Dansereau, O. Pizarro, and S. B. Williams. Linear volumetric focus for light field cameras. *ACM TOG*, 34(2):15, 2015.
- [14] E. R. Dowski and W. T. Cathey. Extended depth of field through wave-front coding. *Applied Optics*, 34(11):1859–1866, 1995.
- [15] T. W. Fahringer, K. P. Lynch, and B. S. Thurow. Volumetric particle image velocimetry with a single plenoptic camera. *Measurement Science and Technology*, 26(11):115201, 2015.
- [16] L. Gao, L. Shao, B.-C. Chen, and E. Betzig. 3d live fluorescence imaging of cellular dynamics using bessel beam plane illumination microscopy. *Nature Protocols*, 9(5):1083–1101, 2014.
- [17] T. Georgiev, K. C. Zheng, B. Curless, D. Salesin, S. Nayar, and C. Intwala. Spatio-angular resolution tradeoffs in integral photography. *Rendering Techniques*, 2006:263–272, 2006.
- [18] P. Green, W. Sun, W. Matusik, and F. Durand. Multi-aperture photography. volume 26, page 68. ACM, 2007.

- [19] M. G. Gustafsson, L. Shao, P. M. Carlton, C. R. Wang, I. N. Golubovskaya, W. Z. Cande, D. A. Agard, and J. W. Sedat. Three-dimensional resolution doubling in wide-field fluorescence microscopy by structured illumination. *Biophysical journal*, 94(12):4957–4970, 2008.
- [20] S. W. Hasinoff and K. N. Kutulakos. Light-efficient photography. *PAMI*, 33(11):2203–2214, 2011.
- [21] S. W. Hasinoff, K. N. Kutulakos, F. Durand, and W. T. Freeman. Time-constrained photography. In *ICCV*, pages 333–340. IEEE, 2009.
- [22] P. J. Keller and M. B. Ahrens. Visualizing whole-brain activity and development at the single-cell level using light-sheet microscopy. *Neuron*, 85(3):462–483, 2015.
- [23] A. Levin. Analyzing depth from coded aperture sets. In *Computer Vision–ECCV 2010*, pages 214–227. Springer, 2010.
- [24] A. Levin, S. W. Hasinoff, P. Green, F. Durand, and W. T. Freeman. 4d frequency analysis of computational cameras for depth of field extension. volume 28, page 97. ACM, 2009.
- [25] M. Levoy and P. Hanrahan. Light field rendering. In *Proceedings of the 23rd annual conference on Computer graphics and interactive techniques*, pages 31–42. ACM, 1996.
- [26] M. Levoy, R. Ng, A. Adams, M. Footer, and M. Horowitz. Light field microscopy. *ACM TOG*, 25(3):924–934, 2006.
- [27] M. Levoy, Z. Zhang, and I. McDowall. Recording and controlling the 4d light field in a microscope using microlens arrays. *Journal of microscopy*, 235(2):144–162, 2009.
- [28] C.-K. Liang, T.-H. Lin, B.-Y. Wong, C. Liu, and H. H. Chen. Programmable aperture photography: multiplexed light field acquisition. *ACM TOG*, 27(3):55, 2008.
- [29] C.-K. Liang and R. Ramamoorthi. A light transport framework for lenslet light field cameras. *ACM TOG*, 34(2):16, 2015.
- [30] X. Lin, J. Wu, and Q. Dai. Camera array based light field microscopy. In *Optical Molecular Probes, Imaging and Drug Delivery*, pages JT3A–48. Optical Society of America, 2015.
- [31] H.-Y. Liu, E. Jonas, L. Tian, J. Zhong, B. Recht, and L. Waller. 3d imaging in volumetric scattering media using phase-space measurements. *Optics express*, 23(11):14461–14471, 2015.
- [32] H.-Y. Liu, J. Zhong, and L. Waller. 4d phase-space multiplexing for fluorescent microscopy. In *SPIE BiOS*, pages 97200A–97200A. SPIE, 2016.
- [33] D. L. Marks, R. A. Stack, D. J. Brady, and J. van der Gracht. Three-dimensional tomography using a cubic-phase plate extended depth-of-field system. *Optics letters*, 24(4):253–255, 1999.
- [34] K. Marwah, G. Wetzstein, Y. Bando, and R. Raskar. Compressive light field photography using overcomplete dictionaries and optimized projections. *ACM TOG*, 32(4):46, 2013.
- [35] J. Mertz. *Introduction to optical microscopy*. Roberts, 2010.
- [36] R. Ng. Fourier slice photography. volume 24, pages 735–744. ACM, 2005.
- [37] R. Ng, M. Levoy, M. Brédif, G. Duval, M. Horowitz, and P. Hanrahan. Light field photography with a handheld plenoptic camera. *Computer Science Technical Report CSTR*, 2(11):1–11, 2005.
- [38] R. L. Nowack. A tale of two beams: an elementary overview of gaussian beams and bessel beams. *Studia Geophysica et Geodaetica*, 56(2):355–372, 2012.
- [39] R. Oldenbourg. Polarized light field microscopy: an analytical method using a microlens array to simultaneously capture both conoscopic and orthoscopic views of birefringent objects. *Journal of microscopy*, 231(3):419–432, 2008.
- [40] N. C. Pégard, H.-Y. Liu, N. Antipa, M. Gerlock, H. Adesnik, and L. Waller. Compressive light-field microscopy for 3d neural activity recording. *Optica*, 3(5):517–524, 2016.
- [41] R. Prevedel, Y.-G. Yoon, M. Hoffmann, N. Pak, G. Wetzstein, S. Kato, T. Schrödel, R. Raskar, M. Zimmer, et al. Simultaneous whole-animal 3d imaging of neuronal activity using light-field microscopy. *Nature methods*, 2014.
- [42] D. Ress, D. Ciarlo, J. Stewart, P. Bell, and D. Kania. A ring coded-aperture microscope for high-resolution imaging of high-energy x rays. *Review of scientific instruments*, 63(10):5086–5088, 1992.
- [43] C. Sheppard and M. Gu. The significance of 3-d transfer functions in confocal scanning microscopy. *Journal of Microscopy*, 165(3):377–390, 1992.
- [44] A. Stern and B. Javidi. Three-dimensional image sensing, visualization, and processing using integral imaging. *Proceedings of the IEEE*, 94(3):591–607, 2006.
- [45] H. Taub and D. L. Schilling. *Principles of communication systems*. McGraw-Hill Higher Education, 1986.
- [46] R. Tomer, M. Lovett-Barron, I. Kauvar, A. Andelman, V. M. Burns, S. Sankaran, L. Grosenick, M. Broxton, S. Yang, and K. Deisseroth. Sped light sheet microscopy: Fast mapping of biological system structure and function. *Cell*, 163(7):1796–1806, 2015.
- [47] A. Veeraraghavan, R. Raskar, A. Agrawal, A. Mohan, and J. Tumblin. Dappled photography: Mask enhanced cameras for heterodyned light fields and coded aperture refocusing. *ACM Trans. Graph.*, 26(3):69, 2007.
- [48] L. Waller, G. Situ, and J. W. Fleischer. Phase-space measurement and coherence synthesis of optical beams. *Nature Photonics*, 6(7):474–479, 2012.
- [49] L.-Y. Wei, C.-K. Liang, G. Myhre, C. Pitts, and K. Akeley. Improving light field camera sample design with irregularity and aberration. *ACM TOG*, 34(4):152, 2015.
- [50] G. Wetzstein, I. Ihrke, and W. Heidrich. On plenoptic multiplexing and reconstruction. *IJCV*, 101(2):384–400, 2013.
- [51] G. Wetzstein, I. Ihrke, D. Lanman, and W. Heidrich. Computational plenoptic imaging. In *Computer Graphics Forum*, volume 30, pages 2397–2426. Wiley Online Library, 2011.
- [52] B. Wilburn, N. Joshi, V. Vaish, E.-V. Talvala, E. Antunez, A. Barth, A. Adams, M. Horowitz, and M. Levoy. High performance imaging using large camera arrays. *ACM TOG*, 24(3):765–776, 2005.
- [53] J. Ye, Y. Ji, W. Yang, and J. Yu. Depth-of-field and coded aperture imaging on xslit lens. In *Computer Vision–ECCV 2014*, pages 753–766. Springer, 2014.
- [54] C. Zhou, S. Lin, and S. Nayar. Coded aperture pairs for depth from defocus. In *ICCP*, pages 325–332. IEEE, 2009.
- [55] C. Zhou and S. Nayar. What are good apertures for defocus deblurring? In *ICCP*, pages 1–8. IEEE, 2009.